Journal Name

ARTICLE TYPE

Cite this: DOI: 10.1039/xxxxxxxxxx

Poroelastic properties of hydrogel microparticles†

Joseph D. Berry,*[a]‡ Matthew Biviano,[a] and Raymond R. Dagastine*[a]¶

Received Date
Accepted Date

DOI: 10.1039/xxxxxxxxxx

www.rsc.org/journalname

Hydrogels can be formed in a number of different geometries depending upon desired function. However, due to the lack of appropriate models required to interpret experimental data, it remains unclear whether hydrogel microparticles have the same poroelastic properties as hydrogel films made with the same components. We perform numerical simulations to determine the universal force relaxation of a poroelastic hydrogel particle undergoing constant compression by a spherical probe, allowing analysis of experimental measurements of hydrogel particle material properties for the first time. In addition, we perform experimental measurements, using colloidal probe Atomic Force Microscopy, of the force relaxation of polyacrylamide films and particles made with identical monomer and cross-linker concentrations. We fit our universal curve to the experimental data in order to extract material properties including shear modulus, Poisson's ratio and solvent diffusivity. Good agreement is found for the shear modulus and Poisson's ratio between the particles and the films. In contrast, the diffusivity of the polyacrylamide particles was found to be about half that of the films, suggesting that differences in the synthesis and homogeneity of the films and the particles play a role in determining transport and subsequent release of molecules in hydrogel particles.

1 Introduction

Hydrogels consist of a cross-linked network of polymers immersed in a solvent, typically water. Hydrogels can exist as large-scale structures such as films ('macrogels'), or as particles ('microgels')[1]. In a hydrogel, solvent molecules are free to migrate through the three-dimensional polymer network, and as a consequence the material can shrink or swell according to external stimuli such as temperature, pH, or ionic strength[1,2]. Because of this property, hydrogel particles have applications in wastewater treatment[3], enhanced oil recovery[4], flavour delivery in foods[5], tissue engineering[6], and biosensing[7].

In particular, hydrogel particles hold great promise for use as controlled drug delivery systems due to their biocompatibility, ease of manufacture, and precise control of strength and size[8–10]. Control of size and strength is critically important for successful delivery of active ingredients *in vivo*. For example, softer particles are able to circulate longer in the bloodstream in comparison to stiffer particles because they can move through narrow vessels, and are also able to avoid detection and subsequent removal by the immune system[11]. Drug delivery to the lungs is critically dependent on particle size and modulus, where particles larger or stiffer than red blood cells are filtered out of circulation[12].

Theory of hydrogel poroelastic response to stimuli was first developed by Tanaka *et al.*[13,14], based upon theory originally formulated by Biot[15] for fluid-saturated porous soil. Characterisation of the poroelastic properties of hydrogels has primarily focussed on films[16–18]. Characterisation typically involves indentation, where an indenter (e.g. sphere, cylinder or sharp tip) is pressed into the sample and held in place, and the subsequent force relaxation of the material is measured over time. Theory is required to interpret the experimental force response in order to quantify important mechanical and transport properties of the gel: the shear modulus G, the diffusivity D (or permeability k), and the drained Poisson's ratio ν_∞.

When an external stimulus is applied to a hydrogel, two distinct mechanisms can govern the response of the gel. The gel can respond *poroelastically*, whereby solvent diffusion through the network is coupled to deformation of the network. In addition, the network can undergo conformational change, resulting in a *viscoelastic* response. Importantly, these effects can be separated by careful choice of experimental length-scale[16,19,20]. The time-scale for poroelastic relaxation is governed by the size of the contact area between the indenter and the gel, as the sol-

[a] *Department of Chemical & Biomolecular Engineering, University of Melbourne, Parkville, Victoria 3010, Australia*

† Electronic Supplementary Information (ESI) available: [details of any supplementary information available should be included here]. See DOI: 10.1039/b000000x/

‡ E-mail: joe.d.berry@gmail.com

¶ E-mail: rrd@unimelb.edu.au

vent has to migrate through the network around the indenter and into solution. In contrast, the viscoelastic time-scale is independent of the contact area and hence systematic variation of contact area size can separate the two time-scales to allow quantification. However, in the case of micron-sized particles, there is no such freedom to choose contact area size in order to separate poroelastic and viscoelastic timescales. Furthermore, in order to link time-scale measurements to physical properties there is no model currently available to correctly interpret experimental force relaxation measurements of purely poroelastic particles.

Recently, finite-element simulations of poroelastic materials have been used to determine universal curves describing the force relaxation in response to fixed-depth and oscillatory indentation, both for thick films and thin films on hard substrates[17,21–23]. The unversal curve directly relevant to indentation of films with a colloidal (spherical) probe was derived by Hu *et al.* [17]:

$$\frac{F(t)-F_\infty}{F_0-F_\infty} = 0.491\exp(-0.908\sqrt{\tau}) + 0.509\exp(-1.679\tau). \quad (1)$$

where F_0 is the instantaneous force response, F_∞ is the equilibrium force response, $\tau = Dt/a^2$ is time normalised with the poroelastic timescale, and a is the contact radius. Fitting the relevant universal curve to the experimental data allows quantification of the mechanical properties of the gel. While shown to be effective for films, this model is not valid to describe the force relaxation of poroelastic particles. This is because compression of a particle involves two indentations: one due to the spherical probe, and the other due to the substrate. As a consequence, solvent drains from two regions of the particle, and there are two (unequal) contact radii and thus two different poroelastic timescales during the compression. Further, the indentation depth measured by the AFM cantilever consists of two contributions from the probe and the substrate, and it can be shown that the effective probe indentation is less than the measured indentation for spherical objects[24,25]. If this is not taken into account, this leads to under-predictions of shear modulus and over-predictions of contact radii.

Measurement of the mechanical and transport properties of hydrogel microparticles using indentation is a difficult experimental task, and several factors constrain the measurement. Firstly, the indentation depths need to be much smaller than the particle and indenter radii to ensure that linear poroelastic theory applies. Secondly, the velocity of the probe as it approaches and indents the particle needs to be fast enough such that negligible solvent has drained from the particle during approach after contact, but slow enough such that elastohydrodynamic effects due to film drainage coupled with deformation[26–29] do not contribute significantly to solvent drainage during approach. Thirdly, the measurement requires accurate estimates of the indentation contact area, and adhesion between the probe and the material can introduce significant deviations from the oft-assumed elastic contact[30]. Lastly, the asymmetry of the indentation due to the presence of a flat substrate needs to be corrected for when indenting particles[24,25].

Microscale indentation has been carried out on polyacrylamide films[30,31], but no similar measurement has been performed on hydrogel microparticles. A very recent approach of promise used microaspiration to extract mechanical and transport properties[32], however there is a requirement for a technique that takes advantage of the force-indentation measurement capabilities of AFM for accurate measurement of mechanical properties and validation of other measurement techniques.

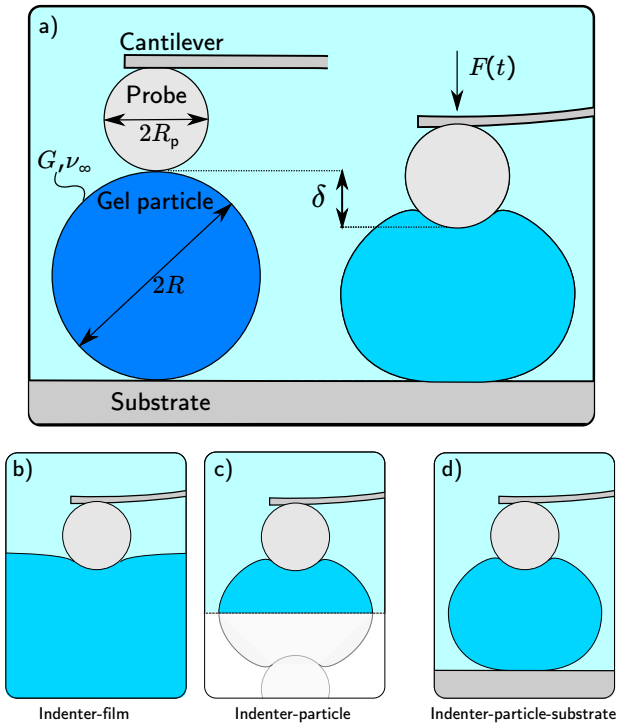

Fig. 1 Schematic showing a) the typical experimental setup for the indentation of a poroelastic particle using Atomic Force Microscopy. A poroelastic particle of radius R is indented by a distance δ with a probe of radius R_p attached to the AFM cantilever. The probe is then held against the particle for a period of time, and the resultant applied force $F(t)$ is measured. The poroelastic particle is characterised by the shear modulus G, the drained Poisson's ratio ν_∞, and the permeability k (or diffusivity D). The three geometries considered in this study are b) a spherical probe indenting a thick poroelastic film, b) the symmetric indentation of a poroelastic particle by spherical indenters (Hertzian geometry), and c) a poroelastic particle resting on a flat substrate undergoing indentation by a spherical probe (AFM geometry).

In this study we use numerical simulations to determine the appropriate universal curve for the compression of a poroelastic particle resting on a flat substrate with a spherical indenter. We then present experimental measurements of polyacrylamide films and particles in order to validate the universal curve, to quantify the physical properties of the film and the particles, and lastly to determine if physical properties differ between microparticles and bulk films made from the same material.

2 Theory & Method

2.1 Numerical model

A schematic of the indentation process is shown in Figure 1. A rigid, spherical probe of radius R_p attached to the AFM cantilever indents a poroelastic particle of radius R by a distance δ. Throughout the indentation process the hydrogel particle is

considered to be in mechanical equilibrium, which is expressed mathematically as:

$$\nabla \cdot \boldsymbol{\sigma} - \frac{1}{\Omega}\nabla\mu = 0 \tag{2}$$

Here μ is the chemical potential, Ω is the volume of a solvent molecule, and $\boldsymbol{\sigma}$ is the standard elastic stress tensor, defined as

$$\boldsymbol{\sigma} = 2G\left[\boldsymbol{\varepsilon} + \frac{\nu}{1-2\nu}\varepsilon_{kk}\boldsymbol{I}\right], \tag{3}$$

where $\boldsymbol{\varepsilon}$ is the strain tensor, ε_{kk} is the trace of the strain tensor, $\boldsymbol{I}$ is the identity matrix, and G and ν are the particle's shear modulus and Poisson's ratio respectively. The strains are defined in terms of the material displacement $\boldsymbol{u}$ as

$$\boldsymbol{\varepsilon} = \frac{1}{2}\left(\nabla\boldsymbol{u} + (\nabla\boldsymbol{u})^T\right) \tag{4}$$

Conservation of mass states that the concentration of solvent is governed by the equation:

$$\frac{\partial C}{\partial t} = \frac{k}{\eta\Omega^2}\nabla^2\mu \tag{5}$$

where C is the number of solvent molecules per unit volume, k is the permeability, and η is the solvent viscosity.

Assuming that the gel is incompressible, the increase in volume of the gel is due entirely to the volume of absorbed solvent:

$$\varepsilon_{kk} = \Omega(C - C_0) \tag{6}$$

where C_0 is the initial concentration.

Combining Equations 5 & 6 gives:

$$\frac{\partial \varepsilon_{kk}}{\partial t} = \frac{k}{\eta\Omega}\nabla^2\mu \tag{7}$$

The diffusivity D is related to other material properties according to:

$$D = \frac{2(1-\nu)Gk}{(1-2\nu)\eta}. \tag{8}$$

Axisymmetric numerical simulations of the indentation process were carried out using the commercial software Comsol Multiphysics (5.2a) through solution of the governing equations 2 & 7 with appropriate boundary conditions. Three different geometries of a poroelastic material undergoing compression were considered in the numerical simulations (Figure 1). The first geometry considered was a spherical probe of radius R_p compressing a thick poroelastic film with constant indentation depth δ, identical to the setup considered by Hu *et al.* [17] (Figure 1b)). The top boundary of the poroelastic material away from the indenter was assumed to be stress free and in equilibrium with the external solvent ($\mu = \mu_0$, where μ_0 is the solvent chemical potential). The indenter was assumed to be impermeable to solvent migration, however because the contact area varies with indentation depth and indenter size we used a Robin boundary condition on the top surface of the poroelastic material to enable a number of simulations to be run with different indentation depths and indenter sizes. The Robin boundary condition used on top surface of the poroelastic material is:

$$\nabla\mu \cdot \boldsymbol{n} = -\bar{k}(\mu - \mu_0)S(p_c), \tag{9}$$

where $\boldsymbol{n}$ is the unit normal to the boundary, $\mu_0 = 10^{-24}$ J is the (nominal) solvent chemical potential[33], p_c is the contact pressure between the indenter and the boundary, and $\bar{k}(\sim 10^{13}$ m$^{-1})$ is an arbitrary large parameter chosen to ensure no-flux in the contact region and $\mu = \mu_0$ elsewhere. The function $S(p_c)$ is a smoothed step function that varies from 0 when the contact pressure is high to 1 when the contact pressure is negligible (Figure S1 in ESI). The bottom boundary of the poroelastic material was set to be no-flux, and was located far enough away (~ 20 radii) from the indenter to have negligible effect on the final result.

The second geometry modelled was the compression of a spherical poroelastic particle of radius R indented by two identical spherical probes at the top and bottom, analogous to the original geometry considered by Hertz[34] (Figure 1c)). For efficiency, only the top indentation was modelled, with a reflection boundary condition applied through the middle of the poroelastic particle. The boundary of the particle was specified as no-flux in the contact region and $\mu = \mu_0$ elsewhere using Eq. 9.

Lastly, the full AFM geometry shown in Figure 1 was modelled, consisting of a spherical poroelastic particle resting on a flat substrate whilst undergoing compression from a spherical probe directly above (Figure 1d)). For this particular geometry, there are two indentations occuring due to the indenter and the substrate[24,25]. Again, the Robin boundary condition was used to ensure that the no-flux condition where the particle is in contact with either the indenter or substrate, and $\mu = \mu_0$ outside the contact region.

In all cases, the indenter was set to move with prescribed displacement δ, and the substrate was fixed in position. The subsequent force F exerted on the indenter was then measured over a period of time. The mesh size was typically 130,000 elements, with appropriate refinement near the indentation regions.

2.2 Materials

Polyacrylamide particles were produced using 40% acrylamide (BioRad Australia), bisacrylamide (BioRad Australia), cyclohexane (AR grade, ThermoFisher), tetramethylethylenediamine (TEMED, Sigma Aldrich), ethanol (ThermoFisher), ammonium persulphate (APS, Sigma Aldrich), phosphate-buffered saline (PBS, Sigma Aldrich), and Span 60 (ChemSupply). For the bulk polyacrylamide gel the same materials were used as well as 3-aminopropyltriethoxy-silane (99%, Sigma Aldrich) and glutaraldehyde (25% solution, Sigma Aldrich) to modify the glass substrate, and diethoxydimethylsilane (99%, Sigma Aldrich) to modify the gel mould. For glassware cleaning sodium hydroxide (Chem-Supply, Australia), 78% nitric acid (Sigma Aldrich) and Labware detergent concentrate (AJAX, ThermoFisher) were used. Deionized water was produced via Milli-Q system (18.2MΩ resistivity, Merck Millipore).

2.3 Polyacrylamide Synthesis

The polyacrylamide particles were produced in the same manner as Gangotra *et al.*[32], where a suspension of acrylamide solution is dispersed into a cyclohexane solution. A 1:9:89:1 bisacrylamide:acrylamide:Milli-Q water:APS ratio was used to generate the particles. These concentrations have been observed to create highly porous polyacrylamide gel networks relative to gels with lower monomer and cross-linker concentrations[35]. Initially we made polyacrylamide gels of ratio 0.5:9.5:89:1, however at this cross-linker concentration we observed both poroelastic and viscoelastic responses to stimulus. Increasing the cross-linker concentration to 10% resulted in gels that exhibited only poroelastic effects.

To generate the emulsions, 10 mL of cyclohexane phase with 1% Span 60 was magnetically stirred in a 25 mL schott bottle, and 1mL of aqueous acrylamide solution was added drop-wise. The solution was shaken vigorously until the droplet size distribution was between 5-20 μm, verified with light microscopy. The solution was then degassed for 20 mins under a 20kPa vacuum while stirring, and 150 mg of TEMED was added to the emulsion. The emulsion was capped and allowed to incubate for 1 hr for full polymerisation of the acrylamide. To extract the particles, the emulsions were then centrifuged for 5 mins at 5000 rpm, and the resultant pellet was then washed and resuspended 5 times, initially in cyclohexane, then ethanol twice and twice with Milli-Q water. To prepare the samples for indentation, glass rounds were then placed in the AFM fluid cells (Asylum Research, CA, USA), filled with PBS solution and several microdroplets of the dispersed polyacrylamide suspension added. These were allowed to settle for 3 hours prior to the experiment, and the solutions exchanged to remove any particles that had not adhered to the slide surface. These were optically checked with light microscopy, and used on the day of preparation.

To create the bulk polyacrylamide gel we followed the procedure of Denisin and Pruitt[35]. Briefly, identical acrylamide solutions to the particle synthesis were made and cast in a PEEK-glass mould onto a glass round. The PEEK-glass mould was made by a flat disk of PEEK with a 1 cm diameter hole cut from the centre, and glued to the glass round with UV-curable resin (Locktite 349, Henkel Australia). The slide without the PEEK ring was then dried and soaked in a solution of acetone and 1% 3-aminopropyltriethoxy-silane for 15 mins, and then soaked in a 1% glutaraldehyde solution for a further 10 mins. The PEEK-glass slide was first dried and then exposed to UV-Ozone (Procleaner, BioForce), and then exposed to the vapor of diethoxydimethylsilane for 1 min to partially hydrophobise the surface. A droplet of the acrylamide solution was then added into the PEEK ring, followed by 10 μL of 10% TEMED solution, and the top slide placed on top. This was then allowed to polymerise for 1 hr, and placed in a petri dish of Milli-Q solution, where the PEEK-glass slide was removed. These were then placed in the fluid cell and covered again with PBS, allowed to equilibrate overnight at 4 C. The samples were left to return to room temperature prior to measurement with AFM. These samples were used within 1 day of preparation.

All glassware was incubated for one hour sequentially with 10% AJAX, 10% Nitric Acid and 10% Sodium Hydroxide solutions, with copious washing of the slides with Milli-Q between incubations.

2.4 Atomic Force Microscopy

The Atomic Force Microscope (AFM) used in these experiments was an Asylum MFP-3D (Asylum Research, CA, USA). Cantilevers used were MLCT-010 tipless cantilevers (Bruker, USA), with ~ 15 μm silica beads attached via micromanipulation with the MFP-3D using 2 part epoxy resin (Super Strength Araldite, Selleys, Australia), which was allowed to dry for 24hrs prior to use. The cantilever spring constants were determined via the thermal method[36], where the inVOLS was determined prior to each measurement, either by observing the constant compliance of the cantilever against the glass surface in the case of the particle measurements, or by observing the thermal oscillations above the sample for the bulk film measurements[37].

All measurements were performed in the MFP-3D fluid cell, using round glass slides for the base. To perform the indentation on the polyacrylamide gels, the AFM tip was first brought into contact with the film or particle, then an indentation depth sweep was undertaken using successive force curves to set loading forces followed by a dwell at that force for a set time. These data were used to determine the appropriate indentation depths for the measurements. The dwells are indentation controlled and done in closed loop mode. Stepped indentation depths were used to reduce overshoot of the indentation depth and also to ensure contact between the probe and the material by minimising elastohydrodynamic effects, thus avoiding inaccurate measurements at short timescales. For further details see Figure S2 in ESI. For the indentations, the velocity of the indentation was set as high as possible to reduce solvent drainage while the probe reached the desired indentation, but low enough to maintain indentation overshoot below 2 nm. This gave a range of velocities of 15 μm/s for small indentations (<1 μm) and 50 μm/s for larger indentations (>2 μm).

2.5 Swelling measurements

The height, width and depth of swollen films in water were measured using calipers. Following this, the films were immersed in 100% ethanol to displace the water and collapse the films. After ten minutes the ethanol was exchanged for fresh ethanol and the films were left overnight. Calipers were again used to measure the relevant dimensions of the unswollen films. For the particles, images were taken of a number of swollen particles in water ($\sim 10-20$), which were then immersed in 100% ethanol for 10 minutes, then in fresh ethanol for a further two hours. Images of the now unswollen particles were taken and then processed to determine the change in radius between collapsed and swollen particles. The swelling ratio λ_0 for both the films and particles was then calculated by dividing the swollen length by the corresponding dry length. Assuming isotropic swelling, the swelling ratios λ_0 of the films and particles were then calculated by dividing the swollen length (thickness or radius, respectively) by the

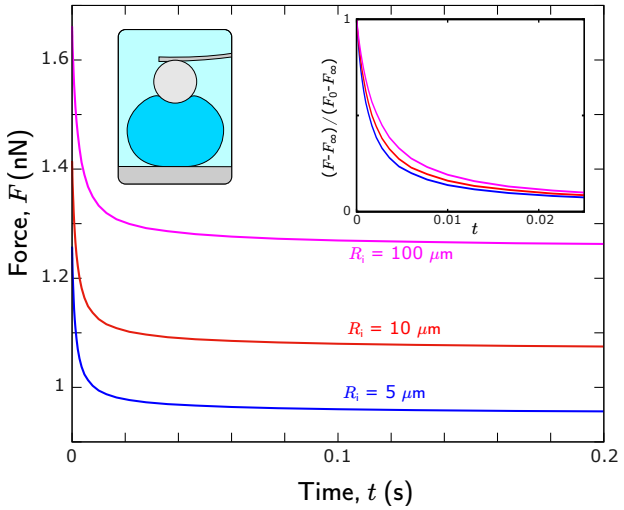

Fig. 2 Effect of probe radius on the simulated force response of a poroelastic particle. The particle of radius 10 μm, resting on a flat substrate, undergoes a constant indentation of $\delta = 20$ nm with different spherical indenter sizes R_p =5, 10, 100 μm. The material parameters are $\nu_\infty = 1/3$, $G = 100$ kPa, $D = 1.5 \times 10^{-11}$ m^2/s. The inset shows the normalised force response as a function of time.

corresponding dry length.

3 Results & Discussion

3.1 Numerical results

The force response of a spherical poroelastic particle resting on a flat substrate by a spherical probe, directly relevant to AFM measurements, is shown in Figure 2 for three different indenter sizes. Initially, the poroelastic material behaves as a purely elastic incompressible material ($\nu_0 = 0.5$), and the measured force at $t = 0$, F_0, is high. As time progresses the solvent drains from the particle, and the force on the indenter decays to a constant equilibrium value $F_\infty < F_0$. The force response of a poroelastic material can be normalised using $(F - F_\infty)/(F_0 - F_\infty)$, an expression that is initially 1, and then decays to 0 as time progresses[17]. This normalisation is plotted against time in the inset of Figure 2, showing that the relaxation time of the poroelastic material increases with indenter size because the distance the solvent migrates is dictated by the size of the contact area, characterised by the contact radius a. Determining the appropriate contact radius for the compression of a particle resting on a flat substrate is complicated because there are two unequal contact areas due to the probe and the substrate.

Figure 3 demonstrates the importance of an appropriate choice of contact radius for particle compression. The simulated force response of a poroelastic material is shown, indented by a spherical indenter of size $R_p = 10$ μm to a depth of $\delta = 20$ nm for the three different geometries considered: a poroelastic film, the symmetric indentation of a spherical poroelastic particle of radius $R = 10$ μm, and the asymmetric indentation of a spherical poroelastic particle (also radius $R = 10$ μm) resting on a flat substrate. Despite being indented by the same indenter by the same distance, the force response of each geometry is different in both the magnitude of the force and the relaxation time. When the indentation depth is small in comparison to the probe radius (and particle ra-

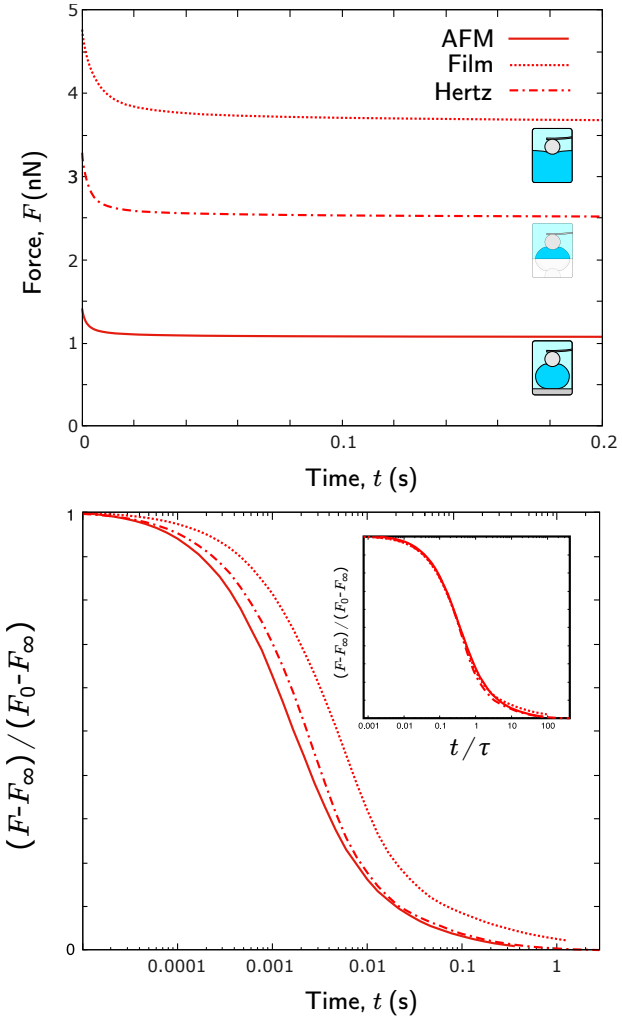

Fig. 3 Effect of geometry on the force response of a poroelastic material for the same indenter size and indentation depth. a) Simulated force response of a poroelastic material undergoing a constant indentation of $\delta = 20$ nm with spherical indenter size $R_p = 10$ μm for the three different geometries considered. b) The same data with force normalised using $(F - F_\infty)/(F_0 - F_\infty)$, where F_0 is the instantaneous force response and F_∞ is the equilibrium force response. The simulations show the force response is highly dependent on the geometry simulated even when force is normalised. The inset in b) shows that the data collapses when time is normalised with the poroelastic timescale $\tau = a^2/D$, where the contact radii a for the film, symmetric and AFM particle indentations are given by Equations 11, 12 & 15 respectively. The material parameters are $\nu_\infty = 1/3$, $G = 100$ kPa, $D = 1.5 \times 10^{-11}$ m^2/s, and the particle radius is 10 μm for the symmetric and AFM particle indentations.

dius if applicable), the force response $F(t)$ at any time t is given by Hertz's theory[34]:

$$F(t) = \frac{8Ga\delta^{\frac{1}{2}}}{3(1-\nu(t))}, \tag{10}$$

where G is the shear modulus, a is the contact radius, and ν is the Poisson's ratio, which changes over time due to drainage of solvent from the material. The contact radius a depends upon the geometry of the indenter and the material. In the case of the film indentation, the contact radius is given by:

$$a_{\text{film}} = \sqrt{R_{\text{p}}\delta} \tag{11}$$

For the symmetric indentation case, the contact radius is given by:

$$a_{\text{symm.}} = \sqrt{\bar{R}\delta}, \tag{12}$$

where $\bar{R} = R_{\text{p}}R/(R_{\text{p}}+R)$ is the effective radius. Because $\bar{R} < R_{\text{p}}$, the contact radius in the film indentation case is larger and the resultant force is larger.

The force in the AFM particle indentation case is much smaller than the other two cases (Figure 3a)). For this particular case, there are two unequal contact areas due to the probe and the substrate, characterised by contact radii a_{p} and a_{s} respectively. The contact radius due to the probe indentation is $a_{\text{p}} = \sqrt{\bar{R}\delta}$, and the contact radius due to the substrate is $a_{\text{s}} = \sqrt{R\delta}$. The reason why the force is smaller for the AFM particle configuration is that the indentation (δ) consists of two contributions: the indentation due to the substrate and the effective indentation due to the spherical probe. Glaubitz *et al.* [24] showed that the effective probe indentation (δ_{p}) required for accurate calculation of material properties can be written as $\delta_{\text{p}} = \hat{C}\delta$, where the factor $\hat{C} \leq 1$ is a correction factor accounting for the presence of the substrate.The factor $\hat{C}$, derived for particles by Glaubitz *et al.* [24] is defined as:

$$\hat{C} = \frac{\delta_{\text{p}}}{\delta} = \frac{[(R_{\text{p}}/R)+1]^{\frac{1}{3}}}{[(R_{\text{p}}/R)+1]^{\frac{1}{3}} + (R_{\text{p}}/R)^{\frac{1}{3}}}, \tag{13}$$

which is a function of the radius ratio R_{p}/R only. Correction factors have also been derived for capsules of arbitrary thickness by Berry *et al.* [25]. The correction factor $\hat{C} \approx 0.56$ for the AFM particle indentation case shown in Figure 3a), and as a consequence the contact radii are less than for the film and the symmetric particle indentation cases even though the applied indentation depth and the probe radius are the same. Thus, the force response of the poroelastic particle resting on a substrate is less than the film and the symmetric cases. Using the correction factor defined in Eq. 13 we can show that the contact radius for the probe and substrate indentations respectively can be written:

$$a_{\text{p}} = \sqrt{\bar{R}\hat{C}\delta}, \quad a_{\text{s}} = \sqrt{R(1-\hat{C})\delta}. \tag{14}$$

To aid comparison, Figure 3b) shows the normalised force response of the three geometries simulated. Here, the variation in contact radii is clear between the three cases, showing that the drainage time increases with increasing contact radius. Previous studies of poroelastic indentation have shown collapse of normalised force data when time is normalised by the poroelastic time-scale $\tau = a^2/D$. The inset of Figure 3b) shows the same data with time normalised by the poroelastic time-scale for each geometry, calculated with the appropriate choice of contact radius (Equations 11 & 12 for the film and symmetric geometries respectively). We found that the contact radius for the AFM particle geometry a_{particle} resulting in the best collapse of the data is the harmonic average of the two contact radii:

$$a_{\text{particle}} = \frac{2a_{\text{p}}a_{\text{s}}}{a_{\text{p}}+a_{\text{s}}}. \tag{15}$$

When the appropriate contact radius is chosen to define the poroelastic time-scale used to normalise time, collapse of the data results (inset of Figure 3b)). Based upon this data collapse, the curve that best fit the normalised force response was found to be

$$\frac{F(t)-F_\infty}{F_0-F_\infty} = 1 - \frac{2.56\tau^{0.94}}{1+2.56\tau^{0.94}}. \tag{16}$$

where the poroelastic time-scale $\tau = a^2/D$ is calculated based on the appropriate choice of contact radius for each geometry:

- Film: $a = a_{\text{film}}$, defined in Equation 11
- Symmetric particle: $a = a_{\text{symm.}}$, defined in Equation 12
- AFM particle: $a = a_{\text{particle}}$, defined in Equations 14 & 15

In Figure 4 we plot the normalised force response of each indentation geometry for three different indenter sizes (and thus three different contact radii), with time normalised by the appropriate poroelastic time scale a^2/D. Also shown for each geometry is the universal curve given by Equation 16. Collapse of the data can be observed when plotted this way, along with excellent agreement between the data and the universal curve. For the film case, we can also compare the only previous analysis for films to the present work, where in Figure 4c) we also plot the fit of Hu *et al.* [17] (Equation 1). Equation 16 fits the numerical data better than Equation 1 for the film indentation simulation results presented here.

The universal curve given in Eq. 16 means that it is now possible to analyse experimental measurements of particle compression in order to to determine the diffusivity D of the hydrogel material.

3.2 Application to experimental measurements

In order to apply Eq. 16 to experimental data, we made polyacrylamide films and particles and performed compression experiments in an AFM using a colloidal probe attached to a cantilever. An example experimental measurement is shown in Figure 5 for a polyacrylamide particle. The drive profile (inset of Figure 5a) consists of three phases: approach, dwell and retract. The corresponding measured force on the cantilever over time is shown Figure 5a), while Figure 5b) shows the more commonly reported force-indentation curve, which does not capture the dynamic time response of the material.

The shear modulus G can be calculated from the approach portion of the force-indentation curve where the indenter is in con-

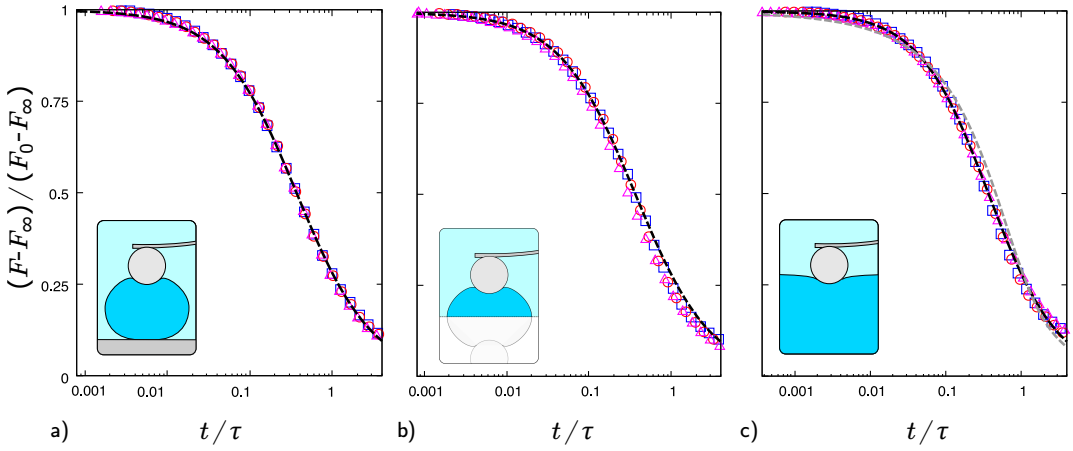

Fig. 4 Comparison of simulation results of the normalised force response as a function of time, normalised by the poroelastic time scale a^2/D, to the universal curve proposed in Equation 16 where the contact radius a is specific to the indentation geometry. a) The asymmetric indentation of a poroelastic particle resting on a flat substrate by a spherical probe (AFM colloidal probe geometry), b) the symmetric indentation of a poroelastic particle by a spherical probe (Hertz geometry), and c) a spherical indenter compressing a poroelastic film. The results of three different indenter sizes for each case are shown: $R_\mathrm{p} = 5$ μm (blue squares), $R_\mathrm{p} = 10$ μm (red circles), $R_\mathrm{p} = 20$ μm (magenta triangles in c)) and $R_\mathrm{p} = 100$ μm (magenta triangles in a) and b)). Also shown are the universal curves derived in the present study (Eq. 16, dashed black line in a) - c)) and in Hu *et al.* [17] (Eq. 1, dashed grey line in c)).

tact with the sample, using Hertz's theory[34]:

$$F_0 = \frac{16}{3} G \bar{R}^{\frac{1}{2}} \delta_\mathrm{p}^{\frac{3}{2}} \tag{17}$$

where the effective indentation depth δ_p can be calculated using the correction given in Equation 13 and the initial Poisson's ratio is $\nu_0 = 0.5$ when the indentation is fast enough that solvent drainage is negligible. An example fit is shown in the inset of Figure 5b). We use the approach data to calculate the shear modulus rather than the retract data, due to the influence of adhesion when retracting. However, the adhesion does not affect the data measured during the dwell phase[30].

The force measured during the dwell period is shown in Figure 5c), along with the universal curve in Eq. 16 used to determine the diffusivity of the sample. Finally, the drained Poisson's ratio ν_∞ can be calculated using the instantaneous and equilibrium force responses of the material undergoing compression (F_0 and F_∞ respectively) with the relation[17]:

$$\frac{F_0}{F_\infty} = 2(1-\nu_\infty). \tag{18}$$

In order to apply the universal curve derived earlier to the experimental data, we first need to ensure that the particles and films are purely poroelastic. Polymer gels can exhibit both viscoelastic and poroelastic effects, where the former is caused conformational changes due to rearrangement of the polymer network and the latter is caused by solvent migration through the polymer network[16,19,20,38]. The time-scale for poroelastic relaxation is governed by the size of the contact area between the indenter and the gel, as the solvent has to migrate through the network around the indenter and into solution. In contrast, the viscoelastic time-scale is independent of the contact area. To confirm that the hydrogel films and particles displayed only poroelastic behaviour, Figure 6 shows the normalised force response of a hydrogel film and particle as a function of time for a number of different indentation depths. When time is not normalised, there is no data collapse over different indentation depths for either the film or particle data, indicating that the response is not viscoelastic. In contrast, when time is normalised with a^2_particle, there is collapse of the data for all indentations shown, demonstrating that the size of the indenter determines the relaxation time of the sample. This confirms that the there is a purely poroelastic response to stimulus for both the film and the particle. The force response of a polyacrylamide film undergoing compression shows excellent agreement with the fitted universal curve derived earlier (Equation 16), shown in Figure 7a). In contrast the universal curve from Hu *et al.* [17] (Equation 1) fails to describe the data as effectively, notably at shorter times.

There is excellent agreement between the experimental force relaxation and the universal curve fit in comparison to the Hu *et al.* [17] curve. For this particular experiment, we measured a shear modulus $G = 7.6$ kPa, a Poisson's ratio $\nu_\infty = 0.36$ and a diffusivity $D = 8.9 \times 10^{-11}$ m^2/s. These properties are in good agreement with previous measurements of polyacrylamide films[30,31].

Extending into geometries that have not been previously modelled or analysed, Figure 7b) shows the force response of a 22.5 μm radius polyacrylamide particle undergoing compression at a smaller indentation depth $\delta = 790$ nm. Again, we see excellent agreement between the experimental data and the universal curve fit. Based on this fit, we calculated a shear modulus $G = 4.8$ kPa, a Poisson's ratio $\nu_\infty = 0.39$ and a diffusivity $D = 2.4 \times 10^{-11}$ m^2/s. For this particular polyacrylamide particle, the shear modulus and the diffusivity are less than that of the polyacrylamide film.

For accurate comparisons and to understand sensitivity to indention depths, we did a range of measurements. For particles we were constrained in our choice of indentation depths in order for linear poroelastic theory to remain valid, whereas the film inden-

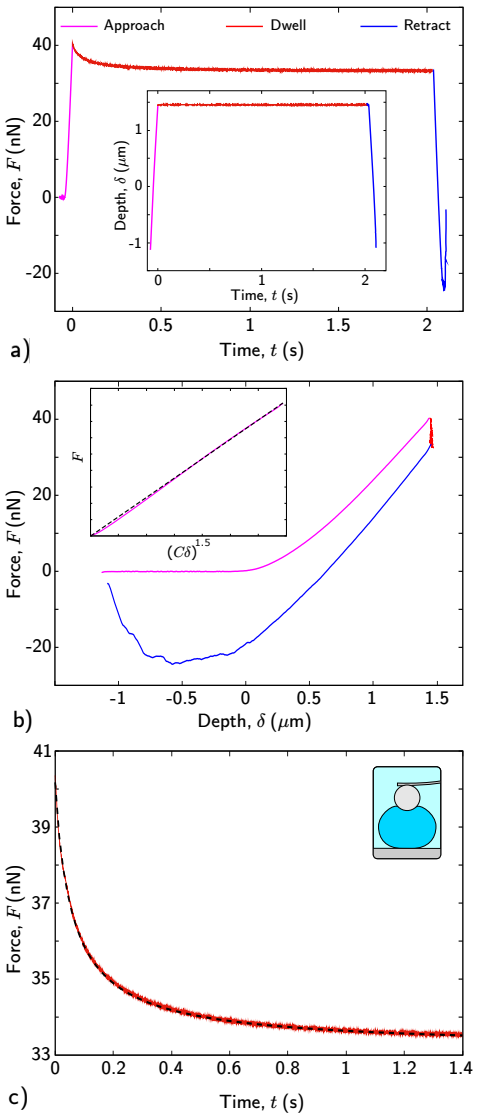

Fig. 5 a) Measured force and indentation depth as functions of time obtained from AFM using a colloidal probe of radius $R_p = 6.35\ \mu$m indenting a polyacrylamide hydrogel particle with radius $R = 22.5\ \mu$m. The inset shows the applied drive profile used to indent the particle to a depth $\delta = 790\ \mu$m. b) The same force and indentation data plotted parametrically to show the more commonly reported force-distance curve. The inset shows the application of Hertz theory (with appropriate correction due to the substrate indentation) used to extract the shear modulus G from fitting the force measured when in contact during approach. c) The same force data plotted as a function of time, measured during the dwell only, along with the best fit of the universal curve (Eq. 16).

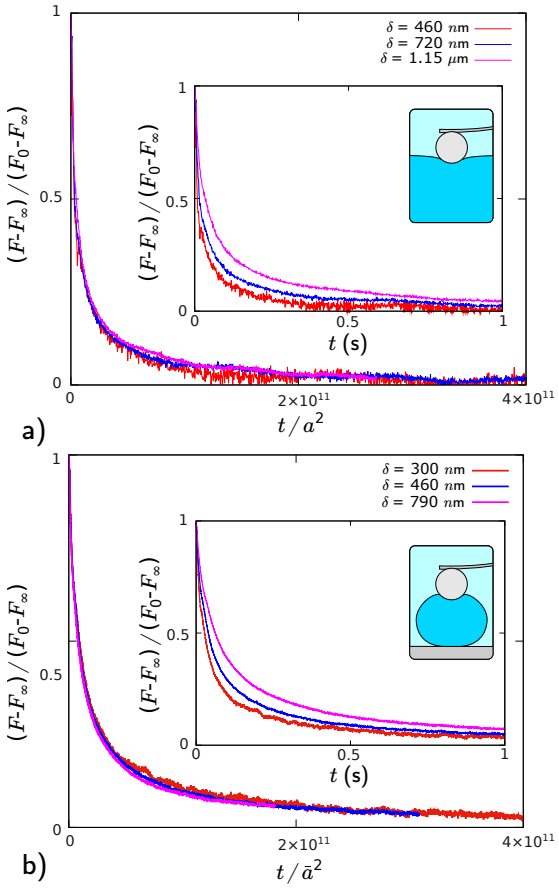

Fig. 6 Experimental data of the normalised force response to different indentation depths for polyacrylamide gel a) films and b) particles, demonstrating that the material response is purely poroelastic, with no viscoelastic relaxation present. Time has been normalised by a^2_{particle}, where the contact radius for the particle is calculated using the harmonic mean of the contact radii of the indentation due to the colloidal probe and the substrate respectively (Eq. 15). The indenter radius is $R_p = 6.35\ \mu$m for both cases, and the particle radius in b) is $R = 27.4\ \mu$m. The same data as a function of time in seconds is shown in the inset of each figure.

tation depths we used were up to an order of magnitude larger. The results are shown in Figure 8 and Table 1, along with the results of Kalcioglu *et al.* [31] who performed similar measurements on polyacrylamide films using indentation depths ranging from 4 μm up to 400 μm. In contrast to the results of Kalcioglu *et al.* [31], who calculate material poroelastic properties by analysing an average force curve compiled from a number of experimental measurements, we analyse each force curve individually and report a range for each property.

Figure 8a) shows that the indentation depths used in this study

Table 1 Mean values of material parameters measured for both films and particles. The standard deviation for each parameter is also shown.

	Shear modulus G (kPa)	Diffusivity D (10^{-11} m^2/s)	Poisson's ratio ν_∞	Permeability k (10^{-18} m^2)	Relaxation time τ (s)	Swelling ratio λ_0
Film	5.7 ± 2.3	8.3 ± 1.5	0.37 ± 0.01	3.3 ± 1.5	0.41 ± 0.34	2.92 ± 0.02
Particle	6.0 ± 2.2	3.6 ± 1.6	0.37 ± 0.03	1.4 ± 1.1	0.08 ± 0.04	2.5 ± 0.3

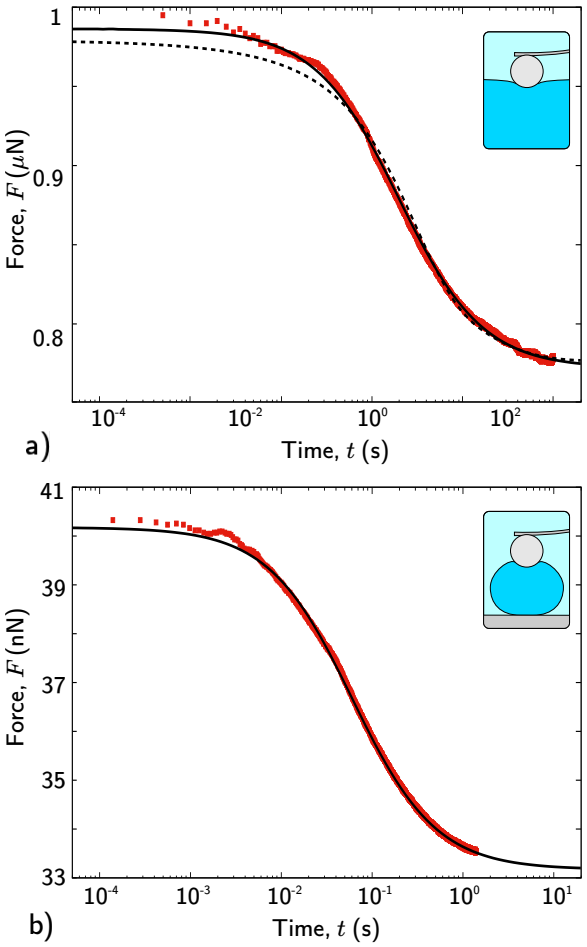

Fig. 7 Comparison of the universal curve given in Equation 16 with the experimental force response as a function of time for a polyacrylamide a) film at an indentation depth $\delta = 3.56$ μm with colloidal probe of radius $R_p = 13.5$ μm, and b) particle of radius 22.5 μm at an indentation depth $\delta = 790$ nm with probe radius $R_p = 6.35$ μm. The solid black line indicates the best fit of Equation 16, and the dashed black line in a) shows the best fit using the expression given in Hu *et al.*[17] (Equation 1)

.

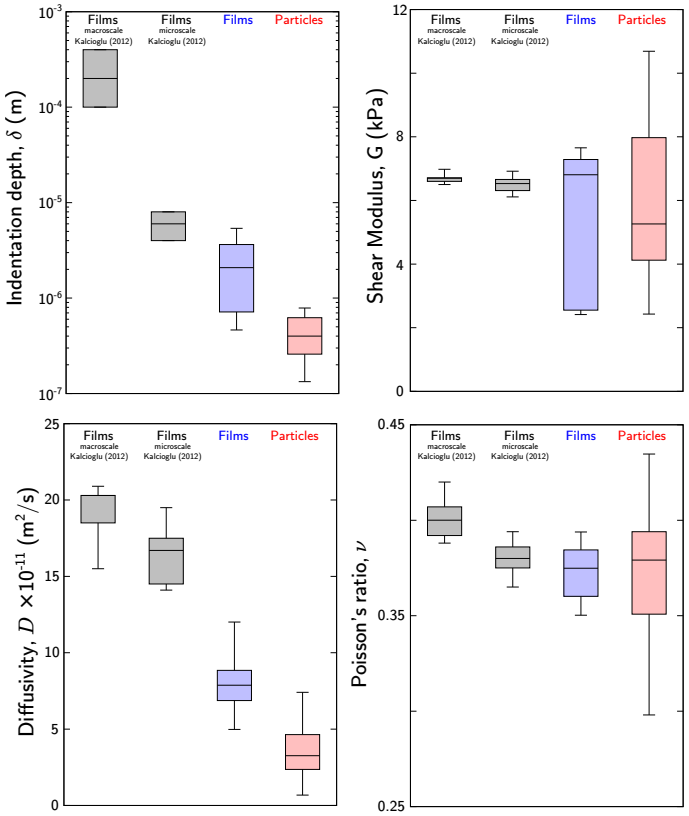

Fig. 8 Analysis of experimental data from this work for polyacrylamide films and particles undergoing constant-depth compression with a spherical indenter compared to the existing film data in the literature. Shown are a) the applied indentation depths, b) shear modulus G, c) diffusivity D, and d) Poisson's ratio ν_∞. The data is displayed as box-plots, where the height of the box represents the data between the first and third quartiles (ie 50% of the data with 25% data below the box and 25% above the box), and the line in the box represents the median value of each quantity. The size of the whiskers represents the entire span of each data-set. The results of film measurements by Kalcioglu *et al.*[31] using instrumented indentation are shown on the left of each plot, their measurements using AFM are second from the left, our measurements of films are second from the right, and our particles measurements are on the right.

at least an order of magnitude less than those used by Kalcioglu *et al.* [31], due to the restrictions imposed by the particle size. For our film measurements, the indentation depths ranged from 460 nm to 5.5 μm, and for the particle measurements we used indentation depths in the range 130 - 790 nm. To our knowledge this is the first time poroelastic properties have been measured using experimental length scales < 1 μm. To ensure an accurate measurement, the solvent cannot drain appreciably during motion of the indenter into the hydrogel. To control for this, we calculate the relaxation time using the calculated diffusivity D and the contact radius a and compare it to the approach time, defined as the time spanning initial contact to maximum force. If the approach time is greater than half the relaxation time, we do not include the result in our final analysis (Fig. S3 in ESI).

Even with the smaller indentation depths used here, surface roughness is not expected to have a significant effect on the analysed data, given that measurements on similar polyacrylamide films yielding roughness values < 1 nm [39]. Despite the disparity in indentation depths, there is good agreement with the measurements of Kalcioglu *et al.* [31] for the shear modulus G and the Poisson's ratio ν_∞ of both films and particles. There is also excellent agreement when comparing the film and particle measurements of both the shear modulus and Poisson's ratio.

There is a significant variation between our diffusivity measurements and Kalcioglu *et al.* [31], who report diffusivities in the range $(1.6-2)\times10^{-10}$ m^2/s. In contrast, we measure lower film diffusivities of $8.3\pm1.5\times10^{-11}$ m^2/s, consistent with the measurements of Lai and Hu [40] using a dynamic indentation profile. This difference can be partly attributed to variations in manufacturing methods and materials, however the key difference between the measurements is the three-stage approach profile we employ for the measurements to reduce overshoots in indentation. An example of this approach is shown in Figure S2, along with a one-stage drive profile. In our approach, we drive the probe at a constant speed (~ 40 μm/s) into contact with the sample, and just before we reach the desired indentation we introduce two short periods of slower velocity before implementing the dwell at constant indentation. This results in an indentation overshoot less than 1%, and importantly the maximum error occurs right at the instant the dwell is initiated, minimising the error in the measurement of the force relaxation. In contrast, the one-stage drive profile results in an overshoot of $\sim 2.5\%$, occurring approximately 10^{-3} s after dwell has been initiated. The larger overshoot may lead to under-estimates of the relaxation time and consequently give over-estimates of the material diffusivity.

There is also a significant difference in the diffusivities measured for films and particles analysed in this study. The particle diffusivities were approximately half that of the film, $D = 3.6\pm1.6\times10^{-11}$ m^2/s. In order to determine whether there are any differences in the size of the polymer network for the films and particles, we measured the swelling ratio of both films and particles. The measured swelling ratios for the polyacrylamide films and particles were 2.92 ± 0.02 and 2.5 ± 0.3 respectively. Lai and Hu [40] recently characterised the diffusivity, along with other properties, of polyacrylamide hydrogels as a function of swelling ratio. Their diffusivity data is shown in Figure 9 along with our particle and film measurements. Our measurements are consistent with the results of Lai and Hu [40], which show an increase in diffusivity with swelling ratio.

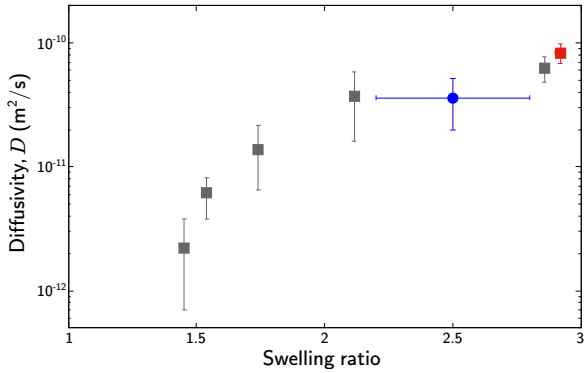

Fig. 9 Diffusivity of polyacrylamide hydrogels as a function of swelling ratio. The grey squares represent measurements on films from Lai and Hu [40]. The red square and the blue circle are the film and particle data from this study respectively.

The difference in swelling ratios between the particles and the film is a result of differences in the fabrication methods. It is unrealistic to expect that one can make a micro-particle in exactly the same way as a bulk film because the reaction and mixing conditions during synthesis will differ. These material differences between geometries emphasise that one must directly measure the material properties of a micro-particle, not of a bulk film made with the same components, in order to precisely characterise the material and subsequently evaluate it suitability to perform required functions. Our results, when compared to the results of Lai and Hu [40], suggest that if the swelling ratios of the films and the particles are similar then the measured diffusivities would also be similar.

In the context of drug delivery *in vivo*, the reduced diffusivity measured for the particles relative to the films is an important result with significant implications. The diffusivity is a measure of how fast molecules can be released from particles in response to external stimuli, of critical importance when considering for example the targeted delivery of drugs *in vivo*. This difference in diffusivities measured here between particles and films means that conclusions regarding transport and release in hydrogel particles cannot be drawn from measurements performed on bulk materials made with the same components.

Estimates of pore size using linear Flory-Huggins theory [38,41,42] based on the swelling ratios measured gives 23 ± 3 nm for the films and 20 ± 3 nm for the particles. Lai and Hu [40] argue that additional cross-linking mechanisms not accounted for in linear Flory-Huggins theory are important in polyacrylamide hydrogels, and instead use a model that assumes the pores are a series of parallel cylindrical tubes along with permeability measurements to predict a pore size ~ 10 nm for the hydrogels considered here. However, the diffusivity of water in similar polyacrylamide hydrogels has been directly measured [43] as $\sim 1.8\times10^{-9}$ m^2/s, which is less than the self-diffusivity of water ($\sim 2.5\times10^{-9}$ m^2/s at 25 C) [44]. This implies that the pore size of polyacrylamide hydrogels is of similar size to that of water molecules (~ 3 Å), much less

than previously predicted.

4 Conclusion

We present the results of numerical simulations of a poroelastic particle undergoing constant compression in order to determine a universal curve of the resultant force relaxation. We demonstrate that the appropriate poroelastic time-scale for a particle resting on a flat substrate undergoing compression by a spherical indenter is the harmonic average of the contact radii due to the indenter and the substrate respectively. In order to validate the universal curve of poroelastic particle compression, we perform experimental measurements, using indentation depths down to 100 nm, on polyacrylamide films and micron-sized particles made with the same components that behave purely poroelastically. In order to avoid overshoot, and to minimise error, we employ a three-stage approach profile prior to dwell at constant indentation. We show that our universal curve is in excellent agreement with experimental measurements of poroelastic particle relaxation. In addition, our universal curve is more accurate than that of Hu *et al.* [17] for the case of films, when applied to experimental measurements of force relaxation.

We fit the universal curve to experimental data to extract poroelastic properties of the polyacrylamide hydrogels, showing good agreement between the films, the particles, and the previous measurements of Kalcioglu *et al.* [31] for both the shear modulus G and the Poisson's ratio ν_∞. We measure film diffusivities that are approximately 50% less than reported by Kalcioglu *et al.* [31], but in agreement with the measurements of Lai and Hu [40] at similar swelling ratios. Lastly we demonstrate that the mean particle diffusivity is approximately half the film diffusivity, possibly due to differences in the synthesis of the films and the particles. As a consequence, care must be taken when extrapolating measurements made on bulk materials in order to draw conclusions regarding the behaviour of poroelastic particles. To avoid misestimations or artefacts, it is advisable to instead directly measure the material properties of a micro-particle, not of a bulk film made with the same components.

With the universal curve presented here for particle compression, it is now possible to quantify the poroelastic properties of biological entities such as cells, which have been shown to behave poroelastically[45], and hydrogel particles for drug delivery *in vivo*[9,12].

5 Acknowledgements

This work was performed in part in the Materials Characterisation and Fabrication Platform (MCFP) at the University of Melbourne and the Victorian Node of the Australian National Fabrication Facility (ANFF). We thank Robert Prud'homme for useful discussions on poroelasticity and hydrogel particles.

References

1 J. B. Thorne, G. J. Vine and M. J. Snowden, *Colloid and Polymer Science*, 2011, **289**, 625–646.
2 M. Murray and M. Snowden, *Advances in colloid and interface science*, 1995, **54**, 73–91.
3 G. E. Morris, B. Vincent and M. J. Snowden, *Journal of colloid and interface science*, 1997, **190**, 198–205.
4 C. Yao, G. Lei, L. Li and X. Gao, *Energy & fuels*, 2012, **26**, 5092–5101.
5 H. M. Shewan and J. R. Stokes, *Journal of Food Engineering*, 2013, **119**, 781–792.
6 P. Panda, S. Ali, E. Lo, B. G. Chung, T. A. Hatton, A. Khademhosseini and P. S. Doyle, *Lab on a Chip*, 2008, **8**, 1056–1061.
7 S. Su, M. M. Ali, C. D. Filipe, Y. Li and R. Pelton, *Biomacromolecules*, 2008, **9**, 935–941.
8 J. P. Best, J. Cui, M. Müllner and F. Caruso, *Langmuir*, 2013, **29**, 9824–9831.
9 N. M. Pinkerton, S. W. Zhang, R. L. Youngblood, D. Gao, S. Li, B. R. Benson, J. Anthony, H. A. Stone, P. J. Sinko and R. K. PrudâĂŹhomme, *Biomacromolecules*, 2013, **15**, 252–261.
10 R. F. Pagels and R. K. Prud'Homme, *Journal of Controlled Release*, 2015, **219**, 519–535.
11 T. J. Merkel, S. W. Jones, K. P. Herlihy, F. R. Kersey, A. R. Shields, M. Napier, J. C. Luft, H. Wu, W. C. Zamboni, A. Z. Wang *et al.*, *Proceedings of the National Academy of Sciences*, 2011, **108**, 586–591.
12 N. M. Pinkerton, S. W. Zhang, R. L. Youngblood, D. Gao, S. Li, B. R. Benson, J. Anthony, H. A. Stone, P. J. Sinko and R. K. Prud'Homme, *Biomacromolecules*, 2014, **15**, 252–261.
13 T. Tanaka, L. O. Hocker and G. B. Benedek, *The Journal of Chemical Physics*, 1973, **59**, 5151–5159.
14 T. Tanaka and D. J. Fillmore, *The Journal of Chemical Physics*, 1979, **70**, 1214–1218.
15 M. A. Biot, *Journal of applied physics*, 1941, **12**, 155–164.
16 M. Galli, K. S. Comley, T. A. Shean and M. L. Oyen, *Journal of Materials Research*, 2009, **24**, 973–979.
17 Y. Hu, X. Zhao, J. J. Vlassak and Z. Suo, *Applied Physics Letters*, 2010, **96**, 2009–2011.
18 M. L. Oyen, *International Materials Reviews*, 2014, **59**, 44–59.
19 D. G. T. Strange, T. L. Fletcher, K. Tonsomboon, H. Brawn, X. Zhao and M. L. Oyen, *Applied Physics Letters*, 2013, **102**, 4–8.
20 Q. M. Wang, A. C. Mohan, M. L. Oyen and X. H. Zhao, *Acta Mechanica Sinica/Lixue Xuebao*, 2014, **30**, 20–27.
21 S. Cai, Y. Hu, X. Zhao and Z. Suo, *Journal of Applied Physics*, 2010, **108**, 1–8.
22 E. P. Chan, Y. Hu, P. M. Johnson, Z. Suo and C. M. Stafford, *Soft Matter*, 2012, **8**, 1492–1498.
23 Y. Lai and Y. Hu, *Soft Matter*, 2017, 852–861.
24 M. Glaubitz, N. Medvedev, D. Pussak, L. Hartmann, S. Schmidt, C. A. Helm and M. Delcea, *Soft Matter*, 2014, **10**, 6732–6741.
25 J. D. Berry, S. Mettu and R. R. Dagastine, *Soft Matter*, 2017, **13**, 1943–1947.
26 F. Kaveh, J. Ally, M. Kappl and H.-J. Butt, *Langmuir*, 2014, **30**, 11619–11624.
27 H.-J. Butt, J. T. Pham and M. Kappl, *Current Opinion in Colloid & Interface Science*, 2016, 82–90.
28 Y. Wang, C. Dhong and J. Frechette, *Physical review letters*, 2015, **115**, 248302.
29 Y. Wang, G. A. Pilkington, C. Dhong and J. Frechette, *Current opinion in colloid & interface science*, 2017, **27**, 43–49.
30 Y. Lai, D. He and Y. Hu, *Extreme Mechanics Letters*, 2019, **31**, 100540.
31 Z. I. Kalcioglu, R. Mahmoodian, Y. Hu, Z. Suo and K. J. Van Vliet, *Soft Matter*, 2012, **8**, 3393.
32 A. Gangotra, M. Biviano, R. R. Dagastine, J. D. Berry and G. R. Willmott, *Soft Matter*, 2019, 7286–7294.
33 M. Li, C. Jin and J. Zhou, *Theoretical and Applied Mechanics Letters*, 2013, **3**, 054009.
34 H. Hertz, *Journal fÂijr die reine und angewandte Mathematik*, 1882, **92**, 156–171.
35 A. K. Denisin and B. L. Pruitt, *ACS Applied Materials & Interfaces*, 2016, **8**,.
36 J. L. Hutter and J. Bechhoefer, *Review of Scientific Instruments*, 1993, **64**, 1868–1873.
37 M. Higgins, R. Proksch, J. E. Sader, M. Polcik, S. Mc Endoo, J. Cleveland and S. Jarvis, *Review of Scientific Instruments*, 2006, **77**, 013701.
38 Y. Hu, X. Chen, G. M. Whitesides, J. J. Vlassak and Z. Suo, *Journal of Materials Research*, 2011, **26**, 785–795.
39 M. Lanniel, E. Huq, S. Allen, L. Buttery, P. M. Williams and M. R. Alexander, *Soft Matter*, 2011, **7**, 6501–6514.
40 Y. Lai and Y. Hu, *Soft Matter*, 2018, **14**, 2619.
41 J. Schurz, *Progress in Polymer Science*, 1991, **16**, 1–53.
42 M. Grassi, C. Sandolo, D. Perin, T. Coviello, R. Lapasin and G. Grassi, *Molecules*, 2009, **14**, 3003–3017.
43 B. Penke, S. Kinsey, S. J. Gibbs, T. S. Moerland and B. R. Locke, *Journal of Magnetic Resonance*, 1998, **132**, 240–254.
44 J. H. Wang, *Journal of Physical Chemistry*, 1965, **69**, 4412.
45 E. Moeendarbary, L. Valon, M. Fritzsche, A. R. Harris, D. a. Moulding, A. J. Thrasher, E. Stride, L. Mahadevan and G. T. Charras, *Nature materials*, 2013, **12**, 253–61.